

Realization of an optimized cylindrical uniform magnetic field coil via flexible printed circuit technology

A-Hui Zhao(赵阿慧), Yong-Le Zhang(张永乐), Yue-Yue Liang(梁跃跃), Yi Zhang(张艺), Jun-Jun Zha(查君君), Dao-Rong Rui(芮道荣), Xiao-Qiang Zhang(张肖强), and Kang Yang(杨康)

Citation: Chin. Phys. B, 2024, 33 (**12**): 120702. DOI: 10.1088/1674-1056/ad84c1
Journal homepage: http://cpb.iphy.ac.cn; http://iopscience.iop.org/cpb

What follows is a list of articles you may be interested in

Response optimization of a three-axis sensitive SERF magnetometer for closed-loop operation

Yuanrui Zhou(周原锐), Yongze Sun(孙永泽), Xixi Wang(汪茜茜), Jianan Qin(秦佳男), Xue Zhang(张雪), and Yanzhang Wang(王言章)
Chin. Phys. B, 2024, 33 (**2**): 020701. DOI: 10.1088/1674-1056/ad0b00

Asymmetric magnetoimpedance effect and dipolar interactions of FINEMET/SiO_2/FePd composite ribbons

Yong-Bin Guo(郭永斌), Dao Wang(王岛), Zhong-Min Wang(王忠民), Lei Ma(马垒), and Zhen-Jie Zhao(赵振杰)
Chin. Phys. B, 2023, 32 (**7**): 070703. DOI: 10.1088/1674-1056/acad6e

A robust method for performance evaluation of the vapor cell for magnetometry

Zhi Liu(柳治), Sheng Zou(邹升), Kaifeng Yin(尹凯峰), Tao Shi(石韬),Junjian Tang(唐钧剑), and Heng Yuan(袁珩)
Chin. Phys. B, 2023, 32 (**4**): 040703. DOI: 10.1088/1674-1056/aca6d5

Improvement of coercivity thermal stability of sintered 2:17 SmCo permanent magnet by Nd doping

Chao-Zhong Wang(王朝中), Lei Liu(刘雷), Ying-Li Sun(孙颖莉), Jiang-Tao Zhao(赵江涛), Bo Zhou (周波), Si-Si Tu(涂思思), Chun-Guo Wang(王春国), Yong Ding(丁勇), and A-Ru Yan(闫阿儒)
Chin. Phys. B, 2023, 32 (**2**): 020704. DOI: 10.1088/1674-1056/ac70b7

General analytical method of designing shielded coils for arbitrary axial magnetic field

Yi Zhang(张燚), Yu-Jiao Li(李玉姣), Qi-Yuan Jiang(江奇渊), Zhi-Guo Wang(汪之国), Tao Xia(夏涛), Hui Luo(罗晖)
Chin. Phys. B, 2019, 28 (**11**): 110702. DOI: 10.1088/1674-1056/ab4d40

Realization of an optimized cylindrical uniform magnetic field coil via flexible printed circuit technology

A-Hui Zhao(赵阿慧)[1,2,3], Yong-Le Zhang(张永乐)[1,2,3], Yue-Yue Liang(梁跃跃)[1,2,3], Yi Zhang(张艺)[1,2,3], Jun-Jun Zha(查君君)[1,2,3], Dao-Rong Rui(芮道荣)[4], Xiao-Qiang Zhang(张肖强)[1,2,3], and Kang Yang(杨康)[1,2,3,†]

[1] *School of Integrated Circuits, Anhui Polytechnic University, Wuhu* 241000, *China*
[2] *Anhui Engineering Research Center of Vehicle Display Integrated System, Wuhu* 241000, *China*
[3] *Joint Discipline Key Laboratory of Touch Display Materials and Devices in Anhui Province, Wuhu* 241000, *China*
[4] *Second Affiliated Hospital of Wannan Medical College, Wuhu* 241000, *China*

(Received 27 June 2024; revised manuscript received 6 September 2024; accepted manuscript online 9 October 2024)

The design and fabrication method of magnetic field coils with high uniformity is essential for atomic magnetometers. In this paper, a novel design strategy for cylindrical uniform coils is first proposed, which combines the target-field method (TFM) with an optimized slime mold algorithm (SMA) to determine optimal structure parameters. Then, the realization method for the designed cylindrical coil by using the flexible printed circuit (FPC) technology is presented. Compared with traditional fabrication methods, this method has advantages in excellent flexibility and bending property, making the coils easier to be arranged in limited space. Moreover, the manufacturing process of the FPC technology via a specific cylindrical uniform magnetic field coil is discussed in detail, and the successfully realized coil is well tested in a verification system. By comparing the uniformity performance of the experimental coil with the simulation one, the effectiveness of the FPC technology in producing cylindrical coils has been well validated.

Keywords: uniform magnetic field coil, optimized target field method, slime mold algorithm, FPC technology

PACS: 07.55.–w, 07.55.Ge, 84.32.Hh, 02.30.Zz **DOI:** 10.1088/1674-1056/ad84c1

1. Introduction

Spin-exchange relaxation-free (SERF) atomic magnetometers are becoming promising sensing units with high sensitivity and accuracy for widespread applications.[1–3] The vital precondition for realizing the SERF state of the atomic spin is a near-zero magnetic field environment.[4] Barker coil,[5] Garrett coil,[6] and Helmholtz coil[7] are commonly used to generate the required uniform magnetic field for residual field suppression, but the structure of these coils is relatively fixed and cannot meet the structural requirements of different applications. Comparatively, a novel coil design strategy based on the target-field method (TFM) introduced by Turner in 1980 brought significant advantages in terms of the flexibility and controllability.[8] Through this method, the shape of the coil can be approximated by discretizing the relevant stream function. Unfortunately, a coarse discretization can lead to severe magnetic field deviation. So intelligent algorithms are often used to handle this problem, such as the simulated annealing (SA) algorithm and particle swarm optimization (PSO) algorithm.[9,10] However, these algorithms always suffer from the problem of local optimum search traps.

Moreover, the fabrication method is critical to the performance of a uniform magnetic field coil. The manual winding method and printed circuit board (PCB) technology are often used to fabricate coils. Whereas, the traditional manual winding method is slow in efficiency and low in precision. And the fixed shape and thickness of the printed circuit board make it difficult to adapt to variations in coil curvatures and dimensions.[11] To overcome these manufacturing limitations, the FPC technology with excellent flexibility and bending property is proposed for cylindrical coils, which allows for higher density and more complex circuit layouts in compact spaces.[12] Nowadays, although the FPC technology is mature, the detailed manufacturing processes are still lacking in the coil manufacturing field for uniform magnetic field.

In this article, based on the theory of the TFM and the slime mold algorithm (SMA), we first present the design and optimization strategy for the cylindrical coil in detail. It is the first time for the TFM and SMA to be combined to determine optimal structure parameters of coil. Then, we explore a process solution based on the FPC technology for a cylindrical coil with high magnetic field uniformity. The performance of the cylindrical coil is analyzed and compared with the theoretical results focusing on the magnetic field uniformity in the target region. The significant advantages of the FPC technology in the manufacture of cylindrical uniform magnetic field coil are demonstrated by the good agreements between the experimental and simulation results.

2. Theory and design

2.1. The theory of target field method

It can be assumed that the uniform magnetic field coil is fixed on the surface of a cylinder with a radius of R and a total

†Corresponding author. E-mail: yangkang@ahpu.edu.cn
© 2024 Chinese Physical Society and IOP Publishing Ltd

height of $2H$ along the z-axis, as shown in Fig. 1. A cube with a side length of L inside the coil is defined as the target region. Note that the centers of the cylinder and cube coincide.

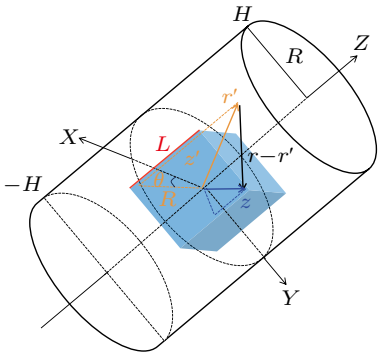


Fig. 1. A schematic diagram of the cylindrical coil. The radius is R and the height is $2H$. The target region is a cube with a side length of L at the center of the coil. The coordinate of the target field point is denoted as $\boldsymbol{r}(X,Y,Z)$ and the coordinate of the source point is denoted as $\boldsymbol{r}'(R,\theta,z)$.

Usually, the current density on a cylindrical surface for a uniform magnetic field can be expressed as a linear combination of trigonometric functions in the cylindrical coordinate system. In order to generate a uniform magnetic field along the radial direction of a cylindrical coil, J_θ and J_z can be expressed as[13]

$$\begin{aligned} J_\theta &= \sum_{n=1}^{N}\sum_{m=1}^{M}\frac{P_{mn}}{m}\cos\left[\frac{n\pi}{2H}(z+H)\right]\sin(m\theta), \\ J_z &= -\frac{2H}{n\pi R}\sum_{n=1}^{N}\sum_{m=1}^{M}P_{mn}\sin\left[\frac{n\pi}{2H}(z+H)\right]\cos(m\theta). \end{aligned} \quad (1)$$

Here, J_θ and J_z are the components of current density $\boldsymbol{J}$ along the θ and z directions, respectively. m and n represent the order of Fourier series terms, whose maximum values are up to M and N. P_{mn} is the expansion coefficient of the current density that needs to be solved.

According to the Biot–Savart's law, the magnetic field generated by the current density can be represented as

$$\boldsymbol{B}(\boldsymbol{r}) = \frac{\mu_0}{4\pi}\iint\frac{\boldsymbol{J}(\boldsymbol{r}')\times(\boldsymbol{r}-\boldsymbol{r}')}{\parallel\boldsymbol{r}-\boldsymbol{r}'\parallel}\mathrm{d}S. \quad (2)$$

The permeability of vacuum is denoted by μ_0. Position vectors of an arbitrary field point and a source point on the coil surface are denoted as $\boldsymbol{r}(X,Y,Z)$ and $\boldsymbol{r}'(R,\theta,z)$ respectively, while $(\boldsymbol{r}$–$\boldsymbol{r}')$ represents the distance between them. And after transforming the coordinate system of the current density, $\boldsymbol{J}(\boldsymbol{r}')$ can be expressed as

$$\boldsymbol{J}(\boldsymbol{r}') = -J_\theta(\theta,z)\sin\theta\boldsymbol{e}_x + J_\theta(\theta,z)\cos\theta\boldsymbol{e}_y + J_z(\theta,z)\boldsymbol{e}_z, \quad (3)$$

where $\boldsymbol{e}_x$, $\boldsymbol{e}_y$, and $\boldsymbol{e}_z$ are unit vectors along the x-axis, y-axis, and z-axis respectively. The three components of the magnetic field then can be obtained by substituting Eq. (3) into Eq. (2). And the radial result along the y-axis can be expressed as

$$B_y(X,Y,Z) = \sum_{n=1}^{N}\sum_{m=1}^{M}Q_{mn}P_{mn}. \quad (4)$$

Here, the coefficient of Q_{mn} is defined as

$$\begin{aligned} Q_{mn} = {} & \frac{\mu_0 R}{4\pi}\int_0^{2\pi}\int_{-H}^{H}\left[\frac{1}{m}\cos\left[\frac{n\pi}{2H}(z+H)\right]\sin(m\theta)\right. \\ & \times(Z-z)\sin\theta \\ & -\frac{2H}{n\pi R}\sum_{n=1}^{N}\sum_{m=1}^{M}\sin\left[\frac{n\pi}{2H}(z+H)\right]\cos(m\theta) \\ & \left.\times(X-R\cos\theta)\right]\times[(X-R\cos\theta)^2 \\ & +(Y-R\sin\theta)^2+(Z-z)^2]^{-3/2}\mathrm{d}z\mathrm{d}\theta. \end{aligned} \quad (5)$$

To generate the desired uniform magnetic field as a constant B_{target}, we need to find a specific solution for this current density. Therefore, in the target region there would be

$$B_y(X,Y,Z) = B_{\text{target}}. \quad (6)$$

However, solving for the undetermined coefficients P_{mn} results in an overdetermined equation when substituting Eq. (4) into Eq. (6). Therefore, an objective function based on the Tikhonov regularization method by introducing a penalty item is usually constructed as follows:

$$E = \sum_{k=1}^{\text{NUM}}[B_y(X_k,Y_k,Z_k)-B_{\text{target}}]^2+\lambda G. \quad (7)$$

Here, NUM represents the total number of target points. λ is the penalty factor to be determined. And P_{mn} then can be solved by setting the derivative of Eq. (7) equalling zero. When P_{mn} is determined, the expression of the stream function can be uniquely derived. And the stream function can be solved according to the following equation:

$$\psi(\theta,z) = \sum_{n=1}^{N}\sum_{m=1}^{M}\frac{2H}{mn\pi}P_{mn}\sin\left[\frac{n\pi}{2H}(z+H)\right]\sin(m\theta). \quad (8)$$

Finally, all the current-carry wires are determined by the contour lines of the stream function

$$\psi(\theta,z) = \psi_{\min}+\left(n-\frac{1}{2}\right)I_0, \quad n=1,2,\ldots,N_{\text{c}}. \quad (9)$$

Note that the total number of turns of the coil is set to N_{c}, and the required current I_0 on each turn can be calculated based on the maximum and minimum values of the stream function

$$I_0 = \frac{\psi_{\max}-\psi_{\min}}{N_{\text{c}}}. \quad (10)$$

2.2. The application of SMA

The penalty factor λ constrains and regulates the windings of the coil design. On the one hand, the larger the value of λ, the smoother the current density distribution of the coil on the surface. On the other hand, an excessively high λ will reduce the magnetic field accuracy in the target region. The value of λ needs to be carefully determined to maintain a balance between the coil smoothness and the magnetic field uniformity, so the SMA is introduced to optimize the values of

λ. It is noteworthy that we combine the SMA with the arithmetic optimization algorithm (AOA) to avoid premature convergence while maintaining a faster convergence rate.[14,15]

Based on the original SMA, the combined algorithm integrates the multiplication and division operator mechanism of AOA for positional updates. Then, the individual position update in the $(t+1)$-th iteration can be described by the following equations:

$$X^{(t+1)} = \begin{cases} r \times (UB - LB) + LB, & r < z, \\ X_{\mathrm{b}}^{(t)} + vb(W \times X_{\mathrm{A}}^{(t)} - X_{\mathrm{B}}^{(t)}), & r < p, \\ X_{\mathrm{b}}^{(t)} / (MOP + \varepsilon) \times ((UB - LB) \times \mu + LB), & p \le r < 0.5, \\ X_{\mathrm{b}}^{(t)} \times MOP \times ((UB - LB) \times \mu + LB), & r \ge p \ \text{ and } \ r \ge 0.5, \end{cases} \tag{11}$$

where r is a random value in the interval of [0, 1]. UB and LB represent the upper and lower boundaries of the slime mold location, respectively. $X_{\mathrm{b}}^{(t)}$ is defined as the individual optimal position in the t-th iteration. vb is a random value in the interval of $[-\mathrm{arctanh}(1 - t/t_{\max}),\ \mathrm{arctanh}(1 - t/t_{\max})]$. t and $t_{\max}$ represent the current and maximum iteration, respectively. $X_{\mathrm{A}}^{(t)}$ and $X_{\mathrm{B}}^{(t)}$ are two random individual locations. μ is the control parameter for adjusting the search process, and ε is a minimum value. MOP denotes mathematical optimizer probability, and the calculation formula is as follows:

$$MOP^{(t+1)} = 1 - \frac{t^{1/\alpha}}{t_{\max}^{1/\alpha}}. \tag{12}$$

The W is designed as the weight of the slime mold, which is used to model the oscillation frequency. The expressions for W and the discriminant factor p can be respectively written as

$$W(i) = \begin{cases} 1 + r \times \log\left(\dfrac{bf - S(i)}{bf - wf} + 1\right), & i < p/2, \\ 1 - r \times \log\left(\dfrac{bf - S(i)}{bf - wf} + 1\right), & i \ge p/2, \end{cases} \tag{13}$$

$$p = \tanh|S(i) - df|, \quad i = 1, 2, 3, \ldots, N_{\mathrm{u}}. \tag{14}$$

Typically, the uniformity error parameter ε_{u} is utilized to assess the performance of the engineered coil. Also, a fitness function F, determined by the maximum absolute value of the uniformity error, acts as a criterion for assessing the effectiveness of the positions from each slime mold

$$F = \max(|\varepsilon_{\mathrm{u}}|), \tag{15}$$

$$\varepsilon_{\mathrm{u}} = \frac{B_y(X_k, Y_k, Z_k) - B_y(0,0,0)}{B(0,0,0)}. \tag{16}$$

Here, B_y (0,0,0) denotes the y-component of the magnetic field at the center of the target region, and the position that achieves the optimum fitness value is indicative of the optimal design parameters.

The flowchart of the optimized SMA-based TFM is shown in Fig. 2. Here, the parameter needs to be optimized is λ. It should be emphasized that optimized SMA improves the ability of SMA to search for optimization in the later stage. The maximum iteration is used as a stopping condition. Once the number of iterations reaches this preset limit, the optimized parameters that correspond to the most favorable position are applied to the objective and stream functions, enabling the realization of an optimal uniform magnetic field coil.

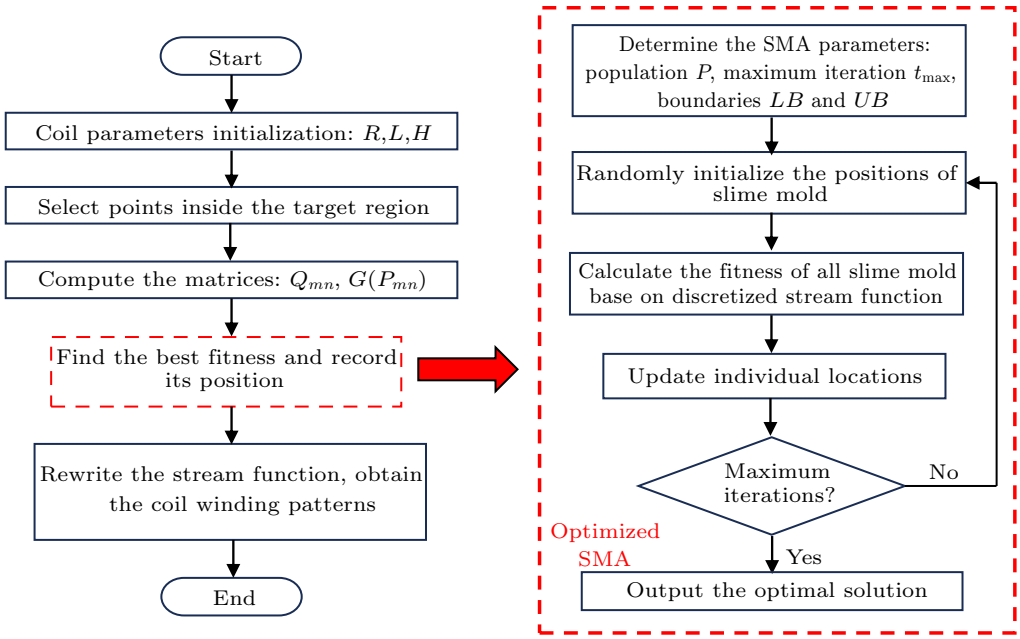


Fig. 2. Detailed flowchart of the optimized SMA used to optimize the TFM for coil design.

3. Simulation and manufacturing

3.1. Simulation results

Restricted by the size of the atomic magnetometer package, the dimension of the coil is limited on a cylindrical surface with a height of up to $2H = 60$ mm and a radius of $R = 12.5$ mm. The target region is a cube with a side length of $L = 8$ mm at the center of the coil. The target points in the target region are selected with a separate distance of 0.8 mm between [−4 mm, 4 mm] in the x, y, and z directions. Therefore, the total point number NUM is 1331.

The M and N are Fourier expansion orders, and their parameters have an important effect on the coil. During the simulation experiments, it was found that the improvement in magnetic field accuracy is not significant when M and N are greater than 5. Therefore, we choose the parameter setting of $M = N = 5$ for the Fourier series.[16] The optimal value of $\lambda = 1.6 \times 10^{-17}$ is determined by the optimized SMA.

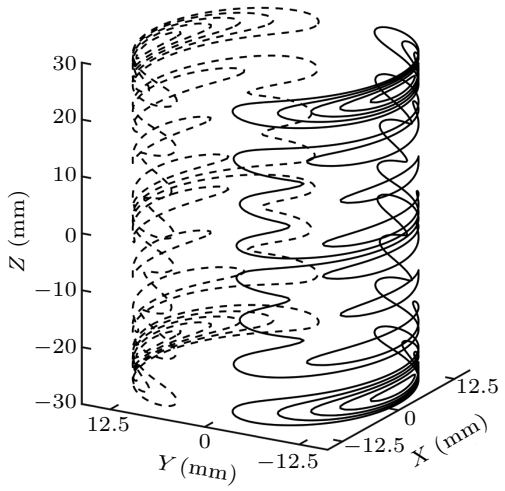


Fig. 3. Winding patterns of the designed coil. The currents in the solid and the dashed coils run clockwise and counter-clockwise, respectively.

Then, the winding patterns of the cylindrical coil can be obtained based on the MATLAB platform, as shown in Fig. 3. To verify the uniformity of the magnetic field generated by the coil, a simulation model is built on the COMSOL platform. As shown in Fig. 4(a), the magnetic uniformity performance is exhibited in the cube with a side length of 8 mm. In the cube target region, the maximum magnetic uniformity error of the coil is less than 0.01. The volume of errors less than 0.005 occupies 79.501% of the entire cube region. In Fig. 4(b), the magnetic field uniformity is demonstrated on the *xoy*, *xoz*, and *yoz* planes within the target region. For both graphs in Fig. 4, the magnetic uniformity errors show a good agreement with both errors limited to 0.01. Practically, uniformity of the magnetic field of the designed coil is satisfactory. Furthermore, to evaluate the performance of the designed coil, the magnetic field along the y-axis of traditional coils is simulated by the COMSOL platform (as shown in Table 1). The volume proportion of $|\varepsilon_u|$ less than 10^{-3} is 22.19% for designed coil, and this proportion is significantly larger than the other coils. Also, the maximum $|\varepsilon_u|$ in the target region is 9.78×10^{-3} (designed coil) and less than other coils. Obviously, the designed coil based on SMA and TFM is superior in providing high uniformity performance.

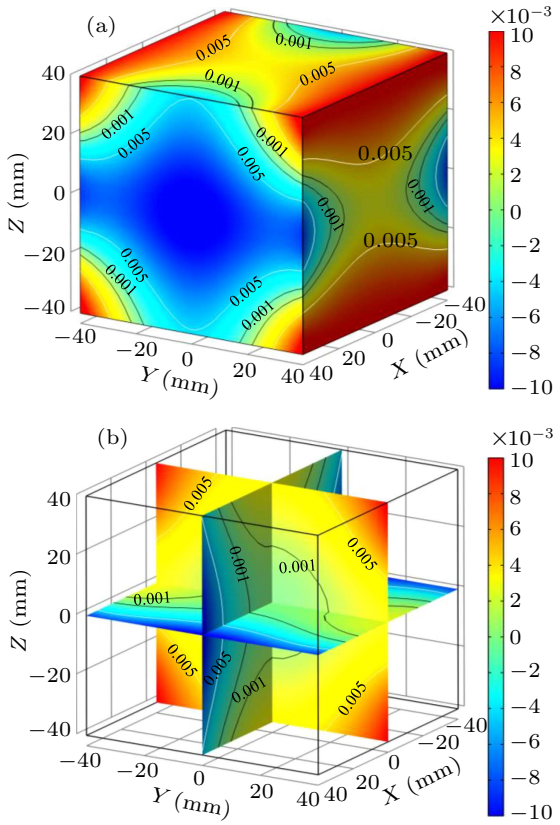


Fig. 4. (a) The distribution of the magnetic uniformity errors in the whole target region. (b) The magnetic uniformity errors on the *xoy*, *xoz*, and *yoz* planes.

Table 1. Maximum and proportion of the uniformity error for different coils.

$\lvert\varepsilon_u\rvert$	Designed coil	Barker coil	Garrett coil	Helmholtz coil
$\leq 10^{-5}$	0.25%	–	–	–
$10^{-5} \sim 10^{-4}$	2.25%	1.08%	0.25%	0.15%
$10^{-4} \sim 10^{-3}$	19.69%	15.43%	2.60%	6.34%
$\geq 10^{-3}$	77.81%	83.49%	97.15%	93.51%
Max	9.78×10^{-3}	5.72×10^{-2}	2.0×10^{-1}	1.79×10^{-1}

3.2. Manufacturing process of coil

Although coils can be manufactured with single-sided FPC technology, the double-sided technology is beneficial to the design of complicated circuits.[12] Therefore, we choose the double-sided FPC technology after considering the complexity of the designed coil. The flexible substrate plays an important role in the manufacturing process of coils, which includes two layers of copper foil and a layer of polyimide (PI) film. The copper foil layer with conductive properties is used to form circuits. Polyimide is a widely used substrate in the FPC industry and has many excellent characteristics, such as high thermal stability and high mechanical strength.[17]

Hence, the PI layer is used to prevent short-circuit phenomena as well as to support the substrate. In this manufacturing process, the copper foil layer with a thickness of 35 μm and the PI film layer of 65 μm are used.

After obtaining the flexible substrate, coil can be manufactured according to the steps shown in Figs. 5(a)–5(i):

Step i: The substrate is coated with an etching solution to remove the oxide layer.

Step ii–iii: The via holes are created in the desired locations by mechanical drilling, and plating through holes (PTH) is used to form a closed metal conductor on the inside of the holes. These holes are employed to achieve the connection between different layers.

Step iv: The coil winding patterns (as shown in Fig. 6) need to be transferred to the copper foil layers. The dry film is attached to the substrate by heating and pressurizing, and the film containing the coil winding patterns is placed over and aligned with the dry film.

Step v: UV-ray is employed to irradiate the dry film and reacts with the dry film that is covered by winding patterns. Meanwhile, the winding patterns are transferred to the dry film layer.

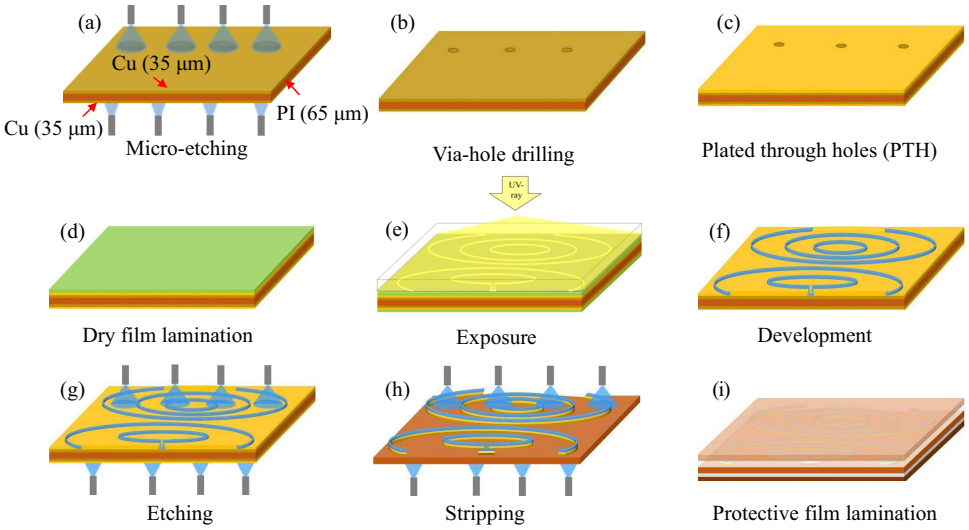


Fig. 5. (a)–(i) The detailed processes for coil manufacturing.

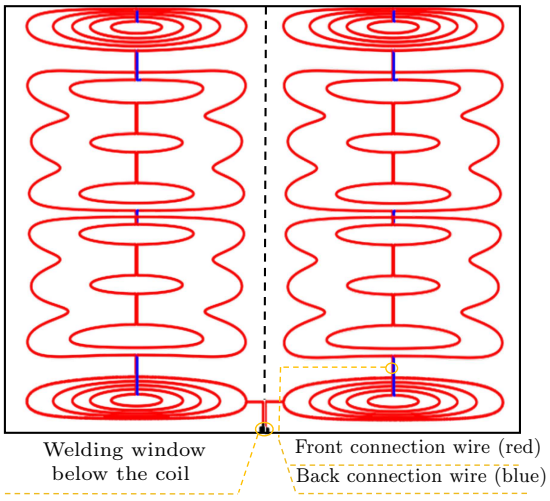


Fig. 6. Design drawings for the coil. The coil is symmetrical on the left and right sides, and the line width set to 1.2 mm. The welding window process is used below the coil.

Step vi–viii: The winding patterns are laminated and formed using the development–etching–strip (DES) processes. The substrate is put into the developing solution to remove the dry film that has not been reacted to by exposure, and the dry film after exposure has been cured without reacting with the solution. The substrate is put into the etching solution to remove the exposed copper foils. After removing the copper foils, only the winding patterns covered by the dry film are left on the substrate. And then the dry film is cleaned off, leaving the desired winding patterns.

Step ix: To protect the circuit, the protective film is laminated to the copper foil layers.

4. Testing and discussion

A testing system is built and its schematic diagram is illustrated in Fig. 7. A signal generator (DG1062Z, RIGOL) applies a voltage signal to a current source (LDC201CU, Thorlabs), which is used to drive the coil. And a flux-gate magnetometer (Mag-13MS100, Bartington Instruments) is used to evaluate the real magnetic distribution of the coil. It needs to be emphasized that the interference of the flux-gate magnetometer to the measured magnetic field is negligible due to its non-magnetic properties. The coil used in the testing system has a length of $2H = 60$ cm and a radius of $R = 12.5$ cm. Compared to the designed coil, the size of the test coil is enlarged 10 times to reduce test difficulty, since the uniformity performance is not affected by the equal scaling operation. The coil is glued on a cylindrical frame which is made of acrylic materials, and placed along the west–south direction in order to reduce interference from the geomagnetic field.

The flux-gate magnetometer is inserted into the test coil to measure the magnetic field at various points along the *y* direction within a range of [−40 mm, 40 mm]. The magnetic field of the test coil is recorded in three axes, as shown in Fig. 8. There are nine test points on the plane, and each of the two adjacent points is separated by a distance of 10 mm. The blue line represents the simulated magnetic uniformity error of the coil. And the measured uniformity error represented by red dots fits the simulated lines well. Furthermore, the simulated errors are not more than 0.004 in these three axes, and the measured error values are within the range of 0.005. The deviation between the measurement and simulation results is within the desired range.

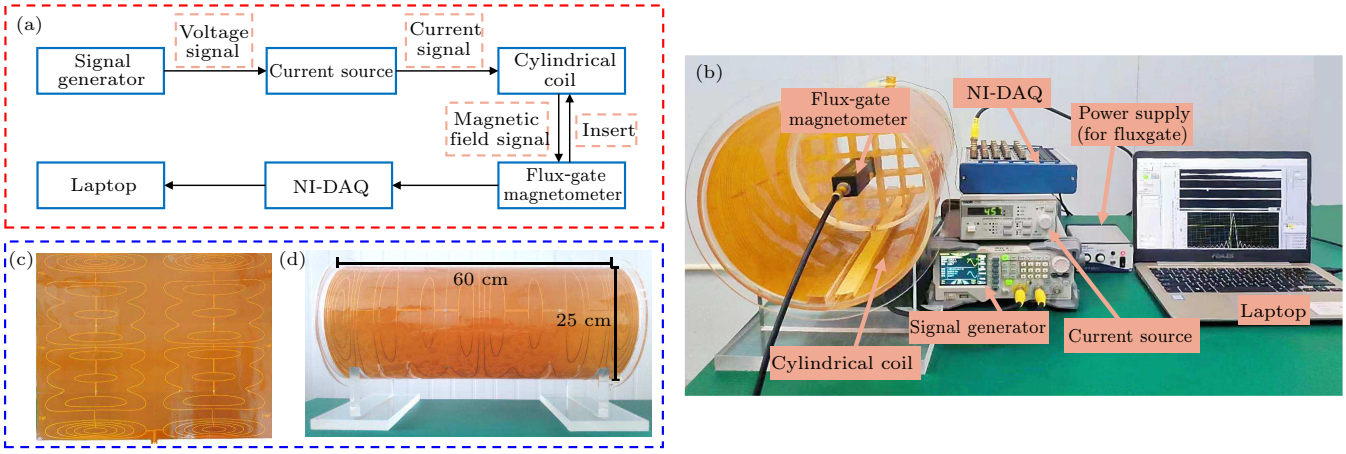


Fig. 7. Experimental test system. (a) Schematic diagram of the testing system, (b) photo of the manufactured coil and its testing system, (c) planar diagram of the manufactured coil, (d) three-dimensional diagram of the manufactured coil.

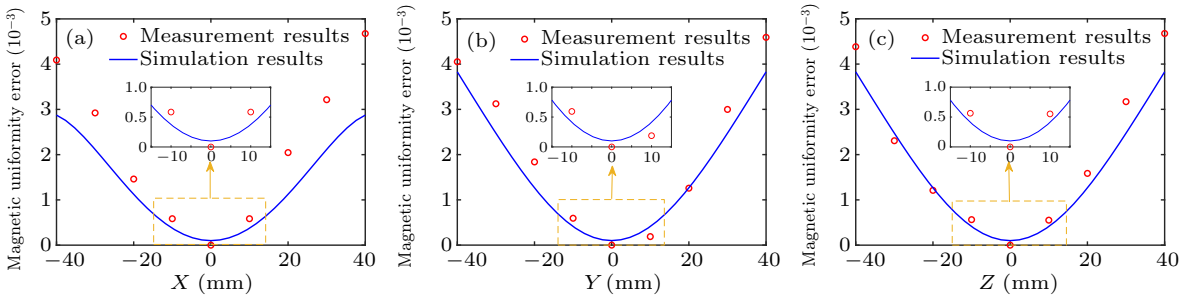


Fig. 8. Simulation and measurement results of the magnetic uniformity error along (a) the *x*-axis, (b) the *y*-axis, (c) the *z*-axis.

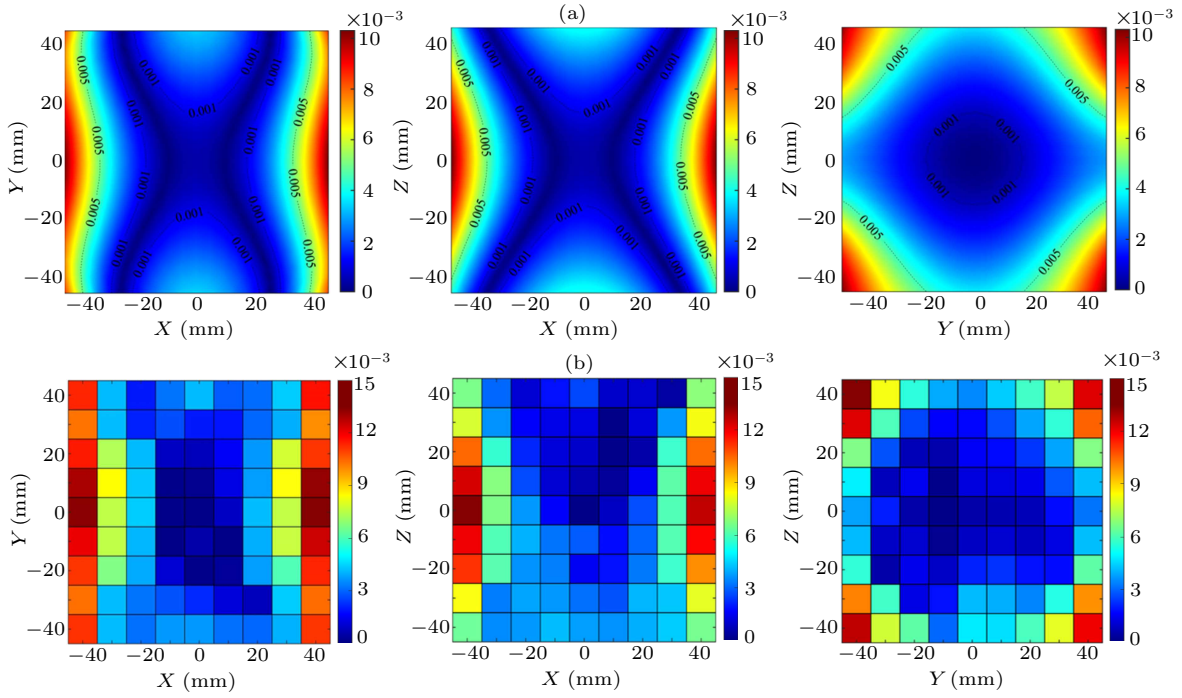


Fig. 9. (a) The simulation results, and (b) the measured results of the magnetic uniformity error distributions on three coordinate planes.

In addition, the magnetic uniformity errors on the three coordinate planes are compared in Fig. 9. In the target region, the simulated uniformity error is less than 0.001, and the corresponding error of the test result is 0.015. The measured magnetic uniformity error value is slightly higher than the simulated value. It can be assumed that additional connection wires, which are designed for uniting all the independent sub-coils in the cylindrical coil, mainly contribute to this deviation. Other errors, such as the alignment error, the reading error and even the drifting error of the current source also play an important role in the disagreement between the simulated and measured results. In the future, additional connection wire, test equipment and test platform will be studied and improved to further reduce the error. Nevertheless, the obtained magnetic field of the manufactured coil still keeps a satisfactory uniformity, which proves the validity of the FPC technology for coil realization.

5. Conclusion

In this paper, the theoretical design method and optimization strategy of this coil is discussed, including the target-field theory and the optimized SMA. Based on the actual coil winding patterns from theoretical analysis, a coil with excellent performance is fabricated using FPC technology. The magnetic uniformity of the coil is well evaluated based on the finite-element simulation method and experimental measurement. The achieved uniformity performance proves the effectiveness of this technology in realizing a complex coil. Moreover, the superiority of the FPC technology also lies in the small wire width of several micro-meters, which is promising for fabricating compensating coils in commercial atomic sensors.

Acknowledgements

Project supported by the National Natural Science Foundation of China (Grant No. 62101004), the Opening Research Fund of Anhui Engineering Research Center of Vehicle Display Integrated Systems (Grant No. VDIS2023C05), the Opening Project of Key Laboratory of Electric Drive and Control of Anhui Province, China (Grant No. DQKJ202309), and the Excellent Scientific Research and Innovation Teams of Anhui Province, China (Grant No. 2022AH010059).

References

[1] Walker T G and Larsen M S 2016 *Adv. At. Mol. Opt. Phys.* **65** 373
[2] Zhang C, Yuan H, Tang Z, Quan W and Fang J C 2016 *Appl. Phys. Rev.* **3** 041305
[3] Wang J, Zhou B Q, Wu W F, Chen L L and Fang J C 2019 *IEEE Sens. J.* **19** 2895
[4] Wang J, Song X, Zhou W Y, Le Y and Ning X L 2021 *IEEE Trans. Ind. Electron.* **68** 11544
[5] Liu Y W, Yang Y, Wang R M and Zhang M 2022 *Meas. Sci. Technol.* **33** 095902
[6] Garrett M W 1951 *J. Appl. Phys.* **22** 1091
[7] Nordahn M A, Holst T and Shen Y Q 1999 *Supercond. Sci. Technol.* **12** 946
[8] Turner R 1986 *J. Phys. D: Appl. Phys.* **19** L147
[9] Han B C, Yang J Z, Zhang X, Shi M X, Yuan S and Wang L 2023 *IEEE Trans. Ind. Electron.* **70** 2057
[10] Zhao F W, Zhou X Y, Xie X X and Wang K 2021 *IEEE Trans. Instrum. Meas.* **70** 1
[11] Taqavi O and Mirimani S M 2020 *IET Electric Power Appl.* **14** 1505
[12] Zhu Y M, Chen X, Chang Y and Yang Z G 2018 *J. Electrochem. Soc.* **165** D494
[13] Wang J, Zhou B Q, Liu X, Wu W F, Chen L L, Han B C and Fang J C 2019 *IEEE Access* **7** 74800
[14] Li S M, Chen H L, Wang M J, Heidari A A and Mirjalili S 2020 *Future Gener. Comput. Syst.* **111** 300
[15] Zhang Y J, Yan Y X, Zhao J and Gao Z M 2022 *IEEE Access* **10** 10907
[16] Yang K, Wu D, Gao W G, Ni T M, Zhang Q N, Zhang H W and Huang D C 2022 *IEEE Trans. Instrum. Meas.* **71** 1
[17] Li L, Yan G P, Wu J Y, Yu X H, Guo Q Z and Kang E T 2008 *Appl. Surf. Sci.* **254** 7331